IOSR Journal of Engineering (IOSRJEN) **www.iosrjen.org**
ISSN (e): 2250-3021, ISSN (p): 2278-8719
Vol. 13, Issue 12, December 2023, ||Series -I|| PP 09-13

Modulate the focusing efficiency of the double-wavelength metalens

Kun Zhao, Qiang Fu, Zhengting Du
School of Physics and Material Engineering, Hefei Normal University, China
Corresponding Author: Kun Zhao
Received 08 December 2023; Accepted 23 December2023

Abstract: Metalenses working in a single wavelength have been very common and can achieve high focusing efficiencies. However, for double or multi-wavelength metalenses, the focusing efficiencies are different at different wavelengths and are not all high. In this letter, we propose a new method to modulate the focusing efficiencies of double-wavelength metalens at both wavelengths, that is, to relax the requirement of the proximity between the phase imposed by the dielectric metalens and the target focusing phase. This method offers a new way for improving the focusing efficiencies on multi-wavelength metasurface design.
Keywords: Metalens, Phase modulation, Focusing efficiency.

I. INTRODUCTION

Metasurface, as a new nanoscale planar component, controls the wavefront by subwavelength scatterers on the interface (Chen et al., 2020), including metallic structures (Zhou et al., 2022) and dielectric elements (Zheng et al., 2022). Dielectric metasurface with low losses have been demonstrated for various optical applications, such as polarization conversion (Yue et al., 2022), focusing (Pan et al., 2022), holographic applications (Wei et al., 2020) and vortex beam generators (Ahmed et al., 2020). Focusing metasurfaces, namely, metalenses, have advantages over conventional lenses due to the miniature and ultrathin characteristics and are easily integrated in optical devices. Metalenses working at a single wavelength have been remarkably demonstrated and can achieve high focusing efficiencies (Khorasaninejad et al., 2016). However, for dual or multi-wavelength metalenses, the focusing efficiencies vary at different wavelengths due to the different response to the same element (Aieta et al., 2015). In the previous work about multi-wavelength metalenses, it was only considered how to adjust the parameters, such as the radius of the nanoposts (Arbabi et al., 2016) and the width of the nanopillars (Shi et al., 2018), to make the elements provide the required phase. It was not considered that if the phase provided by the elements is not so close to the target phase, whether the selected elements can have higher transmittance and thus the focusing efficiencies of the metalens will be improved.

One application of double-wavelength metalens is in the stimulation emission depletion (STED) microscope system. For super-resolution imaging, the fluorescent samples are simultaneously excited by excitation beam with solid focus and depletion beam with doughnut-shaped spot in a STED microscope (Bingen et al., 2011). Traditional STED microscopes generate the two shapes of spots separately, which increases the complexity of the optical systems. It is meaningful to generate the two kinds of spots at different wavelengths on a single layer metalens.

In this paper, we construct a double-wavelength metalens that focuses two different wavelengths into a doughnut-shaped spot and a solid spot respectively as an example and propose a new method to modulate the focusing efficiencies of the dual-wavelength metalens at both wavelengths. The constructed metalens consists of silicon nanobrick arrays with spatially varying size and orientations and it realizes a doughnut-shaped spot at the wavelength of 633nm and a solid spot at the wavelength of 532nm with same right-handed circularly polarized (RCP) incidence. By relaxing the requirement of the proximity between the phase implemented by the dielectric metalens and the required focusing phase, the focusing efficiencies of the doughnut-shaped spot and solid spot can be modulated. Finite different time domain (FDTD) method is applied to obtain the simulation results.

II. METHODS

The constructed metalens of transmission type is illustrated in Fig. 1. Figure 1(a) despicts the metalens focuses the vertically incident RCP plane waves into a doughnut-shaped spot at the wavelength of 633nm and a solid spot at another wavelength of 532nm. Figure 1(b) gives the xy-plane schematic along z direction, indicating changes in both element dimensions and orientation angle. A single unit cell is depicted in the right upper inset.

When a RCP incident plane wave $E_{in}=\begin{bmatrix}1\\-i\end{bmatrix}$ illuminates the unit element in Fig. 1(b), the transmitted field after the element can be described by Jones Matrix as [26]

$$E_{out} = \eta_R|R\rangle + \eta_L e^{-i2\theta}|L\rangle\,, \tag{1}$$

$$\eta_R = \frac{1}{2}\left(t_x e^{i\varphi_x} + t_y e^{i\varphi_y}\right), \tag{2}$$

$$\eta_L = \frac{1}{2}\left(t_x e^{i\varphi_x} - t_y e^{i\varphi_y}\right), \tag{3}$$

where $|R\rangle = \begin{bmatrix}1\\-i\end{bmatrix}$ and $|L\rangle = \begin{bmatrix}1\\i\end{bmatrix}$ denote the RCP and left-handed circularly polarized (LCP) unit vectors respectively. The amplitude transmission of the linearly polarized light along the x and y direction of the element are described by t_x and t_y . φ_x and φ_y are the imposed phase shift accordingly. The transmitted field resolves co-polarized components and cross-polarized components. We base the following design on the second cross-polarized component. The coefficient of the second term represents the phase and transmittance carried by the transmitted left-handed component. The item η_L is related to the length and the width of the silicon nanobrick and can be got by simulation.

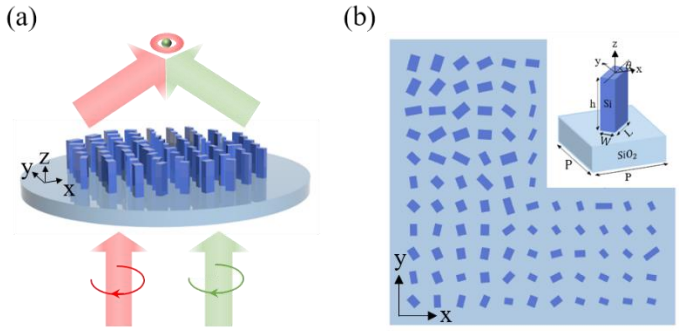

Figure 1: (a) Illustration of the metalens. (b) Top schematic of the constructed metalens.

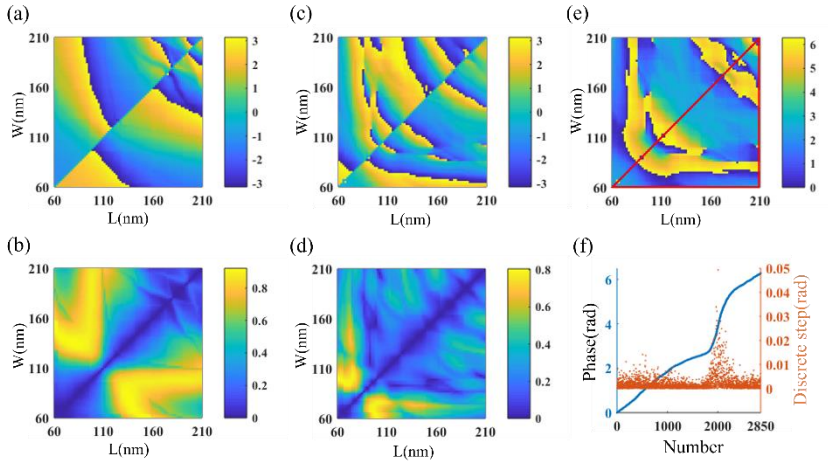

Figure 2: Simulated results of single element.

What should be achieved in a STED microscope are a doughnut-shaped spot at one wavelength and a solid focal spot at another wavelength. We take the hollow spot generated at $\lambda_1 = 633nm$ and the solid spot generated at $\lambda_2 = 532nm$ as examples. Figure 2(a) and (b) show the simulated results of the argument of η_L and the modulus of η_L with the length and the width varying from 60nm to 210nm with the step of 2nm at the wavelength of 633nm. Figure 2(c) and (d) show the corresponding results at the wavelength of 532nm. Periodic boundary conditions along the x and y axes and PML boundary conditions along the z axis are applied on the simulation. The argument of η_L has a range of -π to π. The modulus of η_L is between 0 and 1 and determines the element transmittance. Most values in Fig. 2(d) is low which indicates lower transmittance at $\lambda_2 = 532nm$ than that at $\lambda_1 = 633nm$. For a doughnut-shaped spot at λ_1 , the target phase profile is given by

$$\psi_{\lambda_1}(x,y) = -2\pi/\lambda_1(\sqrt{x^2+y^2+f^2} - f) + l\varphi, \tag{4}$$

where x and y are the coordinates of the nanobricks, f is the designed focal length, l is the topological charge and φ is the azimuthal angle in the polar coordinate. We choose l=1. For λ_2, the target phase profile is given by

$$\psi_{\lambda_2}(\mathrm{x},\mathrm{y}) = -2\pi/\lambda_2\left(\sqrt{x^2+y^2+f^2}-f\right). \quad (5)$$

With given length, width and orientation angle, the silicon nanobrick provides additional phase that is the sum of the argument of η_L and -2θ and the transmittance that is the modulus of η_L according to the coefficient of the second component of Eq. (1). We make the phase imparted by the silicon nanobricks equal to the target focusing phase and get the following equations.

$$\psi_{\lambda_1}(x,y) = Arg\eta_{L_{\lambda_1}}(L,W) - 2\theta, \quad (6)$$

$$\psi_{\lambda_2}(x,y) = Arg\eta_{L_{\lambda_2}}(L,W) - 2\theta, \quad (7)$$

$Arg\eta_{L_\lambda}(L,W)$ denotes the argument of η_L at a chosen wavelength with defined L, W and no rotation. Equation (6) subtracts Eq. (7), we get

$$\psi_{\lambda_1}(x,y) - \psi_{\lambda_2}(x,y) = Arg\eta_{L_{\lambda_1}}(L,W) - Arg\eta_{L_{\lambda_2}}(L,W), \quad (8)$$

where the left side of Eq. (8) gives the difference of the target phase between two wavelengths at fixed point (x,y). The right side of Eq. (8) denotes the needed difference of $Arg\eta_{L_\lambda}(L,W)$ between two wavelengths at point (x, y). Figure 2(e) gives the difference of $Arg\eta_{L_\lambda}(L,W)$ between two wavelengths with various L and W, from which we can see it covers entire 2π range. Due to the symmetry of the Fig. 2(e) along the diagonal, we only use the area surrounded by a red triangle. Arranging all the values in the triangle region from small to large, the blue curve at Fig. 2(f) can be obtained which covers the phase range from 0 to 2π. The number of discrete elements in the triangle region is 2850, which corresponds to the horizontal axis. The differences between two adjacent points on the blue line represent the discrete phase step and are shown by scatter diagram (orange) at Fig. 2(f). Most discrete phase step are below 0.005rad. Back to the Eq. (8), we choose the closest value on the triangle area at Fig. 2(e) to the target value at the left side of Eq. (8) and get suitable L and W of the element. Then we return to Eq. (6) to solve the rotation angle θ at point (x, y).

$$\theta = [Arg\eta_{L_{\lambda_1}}(L,W) - \psi_{\lambda_1}(x,y)]/2. \quad (9)$$

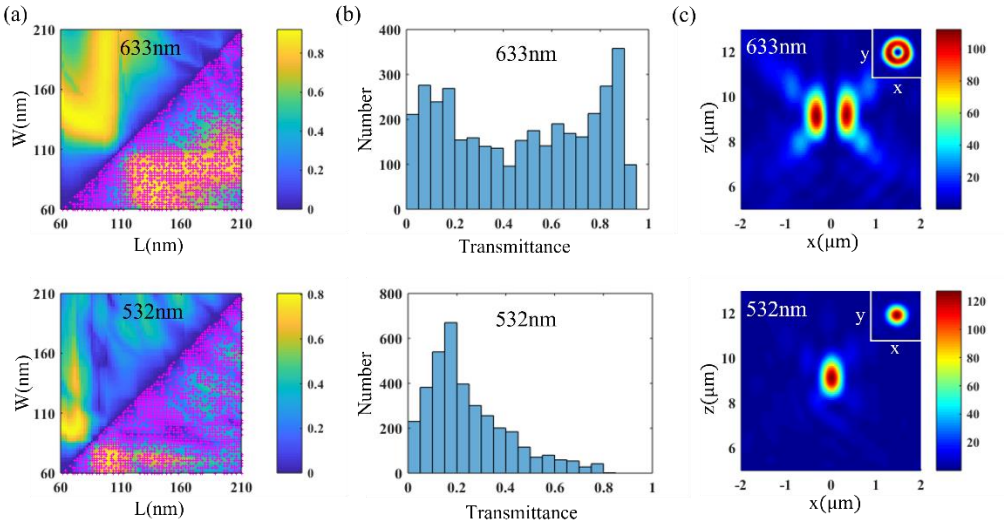

Figure 3: The distribution of all the silicon nanobricks by choosing the closest phase imposed by the silicon nanobricks to the target focusing phase and the simulated intensity profiles in the xz-plane and xy-plane.

Based on above principle, we design a double-wavelength metalens with a diameter of 20μm and the focal length of 10μm. The numerical aperture of the metalens is 0.71. The distribution of the length and width of all the nanobricks on the metalens on the transmittance diagram at the wavelength of 633nm and 532nm are shown in Fig. 3(a). The silicon particles are represented by rose red cross. We can see that the nanobricks are distributed almost in the whole triangle area, including the area with low transmittance. Figure 3(b) give the histogram of transmittance distribution of all the nanobricks on the metalens at the two wavelengths, which clearly shows many nanobricks have low transmittance. The calculated field intensity ($|E|^2$) at xz-plane for RCP incidence at two wavelengths are shown in Fig. 3(c). Maximum intensity is approximately at z=9.1μm , slightly smaller than the design of 10um. This may be due to the limited discretization of the continuous phase profile.

The upper inset in Fig. 3(c) depict the intensity profile of the xy-plane at z=9.1μm. Simulated results clearly demonstrate a doughnut-shaped spot at 633nm and a solid spot at 532nm, which meet theoretical expectations.

However, the focus efficiencies are too small, only 12.6% at 633nm and 2.7% at 532nm. The focusing efficiency is defined as the ratio of the optical power focused to the desired spot to the input power. The diameter of the focal spot is defined as the full width of the normalized intensity at $1/e^2$. The low efficiencies result from the distribution of nanobricks in areas with low transmittance. In the previous design, we choose the length and the width of the element in Fig. 2(e) which can provide the closest phase to the target focusing phase. If we relax the requirement of the proximity between the phase implemented by the silicon nanobricks and the required focusing phase, we can have more nanobricks to choose from at every point (x,y) on the metalens. Choosing the nanobricks with higher transmittance can improve the focusing efficiency.

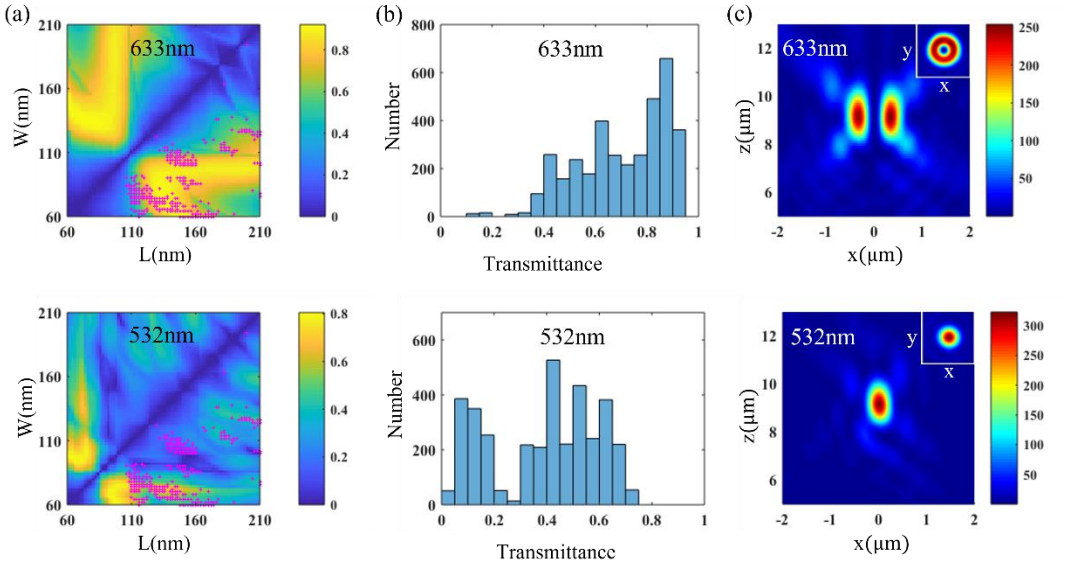

Figure 4: The distribution of the silicon nanobricks by setting the upper limit of phase error as 0.02rad and optimizing the transmittance of the nanobricks at both wavelengths and the simulated intensity profiles in the xz-plane and xy-plane.

Figure 4 shows an example that sets the upper limit of phase error as 0.02rad. The length and width distribution of all the nanobricks on the metalens are shown at Fig. 4(a). We can see that the nanobricks are distributed in some areas where the transmittance is relatively high, rather than throughout the whole area. Figure 4(b) give the histogram of transmittance distribution of all the nanobricks on the metalens at the two wavelengths, which clearly shows the increase in the percentage of nanobricks with high transmittance. The calculated field intensity ($|E|^2$) at xz-plane and xy-plane for RCP incidence at two wavelengths are shown in Fig.4(c). From Fig. 4(c) we can get when the phase requirement is relaxed to 0.02rad error, the focusing efficiencies at both wavelengths can be improved to nearly 2.5 times by selecting appropriate transmittance at both wavelengths.

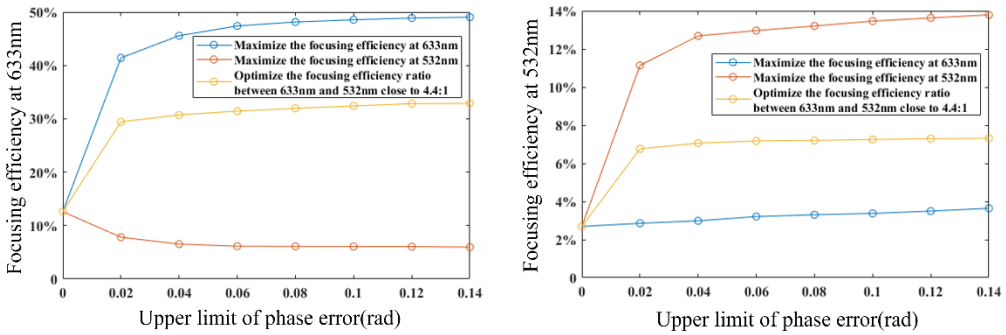

Figure 5: The focusing efficiencies as a function of the upper limit of phase error.

To further analyze the effect of relaxing the phase proximity on the focusing efficiencies in detail, we present the focusing efficiencies curves under three conditions of selecting the transmittance of the silicon nanobricks. The first is that after setting upper limit of phase error, the nanobricks with the highest transmittance at 633nm are selected, which will maximize the focusing efficiency at 633nm. The blue lines in Fig. 5 show the

focusing efficiencies at both wavelengths in this case as the upper limit of phase error increases. We see a significant increase in focusing efficiency at 633nm and it finally becomes flat. Increase in focusing efficiency at 532nm is small. Similarly, if we choose the nanobricks with the highest transmittance at 532nm, the focusing efficiency at 532nm will be maximized. The red lines in Fig.5 show the focusing efficiencies at the two wavelengths in this case with the increase of the upper limit of phase error. We see that the focusing efficiency decreases at 633nm and increases at 532nm with finally being flat. On the above two cases, only the transmittance of the nanobricks at a single wavelength is considered. In order to improve the focusing efficiencies at both wavelengths, we select nanobricks with appropriate transmittance at both wavelengths when the upper limit of phase error is given. As can be seen from the orange lines in Fig.5, the focusing efficiencies at both wavelengths have been significantly improved and finally tend to be flat.

III. CONCLUSION

In conclusion, we design a double-wavelength metalens with adjustable efficiencies. By relaxing the requirement of the proximity between the phase achieved by the dielectric metalens and the target focusing phase, the focusing efficiencies of the doughnut-shaped spot at the wavelength of 633nm and the solid spot at the wavelength of 532nm can be modulated. This method offers a new way for improving the focusing efficiencies on multi-wavelength metasurfaces design.

REFERENCES

[1]. Chen, S., Liu, W., Li, Z., Cheng, H., & Tian, J. (2020). Metasurface-empowered optical multiplexing and multifunction. Advanced Materials, 32(3), 1805912.

[2]. Zhou, Y., Guo, Z., Zhao, X., Wang, F., Yu, Z., Chen, Y.,& Wu, X. (2022). Dual-Quasi Bound States in the Continuum Enabled Plasmonic Metasurfaces. Advanced Optical Materials, 10(19), 2200965.

[3]. Zheng, C., Li, J., Liu, J., Li, J., Yue, Z., Li, H.,& Yao, J. (2022). Creating longitudinally varying vector vortex beams with an all-dielectric metasurface. Laser & Photonics Reviews, 16(10), 2200236.

[4]. Yue, Z., Li, J., Liu, J., Li, J., Zheng, C., Wang, G., & Yao, J. (2022). Versatile polarization conversion and wavefront shaping based on fully phase-modulated metasurface with complex amplitude modulation. Advanced Optical Materials, 10(16), 2200733.

[5]. Pan, M., Fu, Y., Zheng, M., Chen, H., Zang, Y., Duan, H., & Hu, Y. (2022). Dielectric metalens for miniaturized imaging systems: progress and challenges. Light: Science & Applications, 11(1), 195.

[6]. Wei, Q., Huang, L., Zhao, R., Geng, G., Li, J., Li, X., & Wang, Y. (2022). Rotational multiplexing method based on cascaded metasurface holography. Advanced Optical Materials, 10(8), 2102166.

[7]. Ahmed, H., Kim, H., Zhang, Y., Intaravanne, Y., Jang, J., Rho, J., & Chen, X. (2022). Optical metasurfaces for generating and manipulating optical vortex beams. Nanophotonics, 11(5), 941-956.

[8]. Khorasaninejad, M., Chen, W. T., Devlin, R. C., Oh, J., Zhu, A. Y., & Capasso, F. (2016). Metalenses at visible wavelengths: Diffraction-limited focusing and subwavelength resolution imaging. Science, 352(6290), 1190-1194.

[9]. Aieta, F., Kats, M. A., Genevet, P., & Capasso, F. (2015). Multiwavelength achromatic metasurfaces by dispersive phase compensation. Science, 347(6228), 1342-1345.

[10]. Arbabi, E., Arbabi, A., Kamali, S. M., Horie, Y., & Faraon, A. (2016). Multiwavelength polarization-insensitive lenses based on dielectric metasurfaces with meta-molecules. Optica, 3(6), 628-633.

[11]. Shi, Z., Khorasaninejad, M., Huang, Y. W., Roques-Carmes, C., Zhu, A. Y., Chen, W. T., & Capasso, F. (2018). Single-layer metasurface with controllable multiwavelength functions. Nano letters, 18(4), 2420-2427.

[12]. Bingen, P., Reuss, M., Engelhardt, J., & Hell, S. W. (2011). Parallelized STED fluorescence nanoscopy. Optics Express, 19(24), 23716-23726.